Untangling product selectivity on clean low indexed rutile TiO2 surfaces using first-principles calculations

Journal:	*Physical Chemistry Chemical Physics*
Manuscript ID	CP-ART-10-2022-004939.R2
Article Type:	Paper
Date Submitted by the Author:	15-Dec-2022
Complete List of Authors:	Malik, Anum Shahid; Lehigh University, Department of Chemistry Fredin, Lisa; Lehigh University, Lisa Fredin;

SCHOLARONE™
Manuscripts

Untangling product selectivity on clean low indexed rutile TiO$_2$ surfaces using first-principles calculations

Anum Shahid Malik, Lisa A. Fredin[*]

Department of Chemistry, Lehigh University, Bethlehem, PA 18015, USA.

*lafredin@lehigh.edu

Abstract

Computational modeling of metal oxide surfaces provides an important tool to help untangle complex spectroscopy and measured catalytic reactivity. There are many material properties that make rational catalytic design challenging, and computational methods provide a way to evaluate possible structural factors, like surface structure, individually. The mechanism of water oxidation or oxygen evolution is well studied on some anatase surfaces and the rutile TiO$_2$ (110) surface but has not yet been mapped on other low-index Miller rutile surfaces that are present in most experimental nano-titania catalysts. Here first principles calculations provide new insights into water oxidation mechanisms and reactivity of the most common low-index Miller facets of rutile TiO$_2$. The reactivity of three surfaces; (101), (010), and (001); are explored for the first time and the product selectivity of multistep electron transfer on each surface is compared to the well-studied (110) surface. Density functional theory shows that a peroxo, O$^{(p)}$, intermediate is more favorable for water oxidation on all facets. The •OH radical formation is favored on the (001) facet resulting in a high overpotential for oxygen evolution reaction (OER). The (101) and (110) facets have low overpotentials, ~ 0.3 V, and favored two-electron proton-coupled electron transfer to produce H$_2$O$_2$. The only facet that prefers direct OER is (001), leading to O$_2$ evolution in a four-electron process with an overpotential of 0.53 V. A volcano plot predicts the selectivity and activity of low-index Miller facets of rutile TiO$_2$, revealing the high activity of the peroxo OER mechanism on the (010) facet.

1. Introduction

Photocatalytic water splitting via solid-state materials might provide an inexpensive way to generate energy from renewable resources.[1–3] Early active photocatalysts were developed using sacrificial reagents for either H_2 or O_2 evolution.[4] However, discovering the ideal material capable of spontaneously achieving the two reactions remains a major challenge. In particular, semiconductor-based photocatalysts with multiple facets allow important properties to be tuned, like light absorption, mobility of charge carriers, and their driving force to the water solution.[5–8] An ideal material will have a large enough band gap to absorb a large amount of sunlight,[9,10] while the valence band maximum (VBM) and conduction band minimum (CBM) must lie energetically below O_2/H_2O and above H^+/H_2 potentials to drive holes for water oxidation and electrons for reducing H^+, respectively.[11]

Titanium dioxide (TiO_2) is one of the most used materials in heterogeneous photocatalysis because of its strong stability under different conditions.[12,13] Rutile TiO_2's wide band gap of 3.0 eV, makes it a UV light-responsive material, and the number of different stable facets allow for a range of activity for different reactants.[14,15] The overpotential of multiple water oxidation mechanisms has been investigated on the rutile TiO_2 (110) surface, which is considered to be the most stable facet.[16–18] Specifically, the amount of energy required to drive each step beyond the equilibrium potential, known as overpotential,[19–22] provides a good metric of surface reactivity. The photo-oxidation of water on defect-free rutile (110) surfaces has been broadly explored,[19,21,23–31] as well as, direct prediction of OER on rutile (110) with subsurface oxygen vacancies,[32–42] multiple surface coverages,[19,29,43,44] and metal nanoclusters [45–50] adsorbed on the surface provides a detailed picture of its reactivity.

In contrast, other terminations of rutile TiO_2 that are experimentally accessible and have received much less attention. In particular, understanding the photocatalytic activity, especially the effect on yields, rates, or selectivity, of the lower index surfaces has been largely overlooked.[51] Initially, these surfaces were not explored by computational scientists because surface energy calculations show that they are less stable than the (110) surfaces, with stability decreasing (100)[52–54] > (101)[55–58] > (001),[58–61] which is correlated to the density of undercoordinated surface sites.[18] A recent article that calculated the electronic structures of hydroxylated low-index surfaces of rutile and anatase titanium dioxide, suggested that

hydroxyl-bridged surfaces have a lot of potential for photo-electrocatalysis but did not directly assess the catalytic performance of these low-index facets.[62] In the absence of studies identifying the role of each crystal facet in photocatalytic redox reactions, the understanding of photo-oxidation of water by nano-titania is incomplete as only 64% of particle surfaces are (110).[63–65] Thus, computational studies that can separately calculate the properties of each surface are critical to understanding the reactivity of experimental nanostructures.

An important consideration whenever generating models of catalytic surfaces is the stability of those surfaces, especially under catalytic conditions. It is well known that some low-index facets of anatase TiO_2, in particular (101),[66] reconstruct significantly. In general, very little surface reconstruction is seen when rutile surfaces are optimized using DFT.[18] However, while rutile is a more stable phase in general, there is experimental evidence for the reconstruction of atomically flat rutile (001) above 750ºC.[67] This is not surprising as stochiometric (001) has a surface step edge. This edge in the <001> can either be a row of in-plane Ti atoms[68] or in-plane oxygen rows.[69] Scanning tunneling microscopy has shown that the (001) rutile surfaces synthesized have bright rows on the surface[70] that can be assigned to the surface oxygen rows. When (001) rutile surfaces terminated with in-plane oxygens rather than raised bridging oxygens have been optimized no reconstruction is observed.[23]

A second structural consideration in modeling metal oxide catalysis is atomic vacancies observed in experimental materials.[54–56,71–74] Due to the minimal surface disorder seen in rutile crystals and DFT, most studies of rutile,[75–77] both (110) and other surfaces, focus on oxygen vacancies and surface coverages.[78,79] When adsorbed species are more stable than bare surfaces, this type of surface coverage can be thought of as a surface reconstruction. Typically, the dissociation of species on surfaces in a water environment are adsorbed oxygen species like hydroxyl-bridges.[62] Before computational effort is invested in fully exploring the reactivity of other low-index surfaces of rutile TiO_2, a detailed understanding of the complex oxidation of water on each stoichiometric surface is required.

Of the two half-reactions of water splitting, the oxidation step is the most challenging due to the coupling of 4 electron and proton transfers and the creation of an oxygen-oxygen (O_2) bond.[80] One major issue contributing to catalytic inefficiency is side reactions leading to unproductive products or products that directly block active sites. In particular, water

oxidation could lead to •OH radicals, H_2O_2, or O_2 evolution electrochemically or photoelectrochemically.[20] These three half-cell reactions that lead to the above-mentioned products depend on the number of electrons transferred, 1, 2, or 4 electrons. The formation energy of •OH in the aqueous phase from H_2O (Eqn. 1) at pH = 0 is 2.4 V. [81] When $\Delta G_{OH*} >$ 2.4 eV, water oxidation occurs via the one-electron process resulting in the formation of unproductive •OH. In a two-electron process, the amount of energy required for the production of H_2O_2 in the aqueous phase (Eqn. 2) is 1.76 V.[82] When $\Delta G_{OH*} < 2.4$ eV and $\Delta G_{O*} > 3.5$ eV at pH = 0, H_2O_2 is formed. If $\Delta G_{OH*} < 2.4$ eV and $\Delta G_{O*} < 3.5$ eV at pH = 0, water oxidation would undergo the four-electron process to the desired O_2 evolution. The required energy for the production of O_2 in the aqueous phase from H_2O is 1.23 V.[82]

$$H_2O \rightarrow \text{•OH} + (H^+ + e^-) \tag{1}$$

$$2H_2O \rightarrow H_2O_2 + 2 (H^+ + e^-) \tag{2}$$

$$2H_2O \rightarrow O_2 + 4 (H^+ + e^-) \tag{3}$$

This work uses computational catalytic tools to predict solar-to-chemical energy conversion on the four low-index Miller surfaces of rutile TiO_2, (110), (101), (010), and (001) (Figure S1). First-principle calculations can predict the redox potentials of multielectron proton-coupled electron transfer mechanisms on each facet. Unlike experimental reactivity, density functional theory (DFT) allows the mechanism through two distinct reactive intermediates, *i.e.,* dangling O* and surface-bound peroxo O* denoted as $(O^{(d)})$ and $(O^{(p)})$, to be examined separately. The structure of each surface and the intermediates and thermodynamic analysis of the free energy for the three possible products, *i.e.,* •OH/H_2O_2/O_2, provide insights into the selectivity of these understudied surfaces. This work provides experimentalists with design guidelines for faceted TiO_2 crystalline nanomaterials that should enhance photocatalytic water oxidation by identifying the most suitable facets for OER and criteria for product selectivity.

2. Computational Methodology

Spin-polarized density functional theory (DFT) characterized the intermediates for OER activity of the rutile TiO_2 (001), (101), (110), and (010) surfaces. For the structure determination, the Perdew−Burke−Ernzer (PBE) parameterizations of the exchange and

correlation potential in the generalized gradient approximation (GGA)[83] as applied in the Vienna Ab-Initio Simulation Package (VASP) code was adopted.[84,85] To expand the electronic wave function, and valence configurations of the atoms: $3s^2 3p^6 4s^2 3d^2$ for Ti's (12 valence electrons), $2s^2 2p^4$ for O's (6 valence electrons), and $1s$ for H (1 valence electron) with PAW potentials to account for the core electrons a plane-wave energy cutoff of 400 eV was applied. The self-consistent DFT energies convergence criterion was 10^{-4} eV with a force on each atom of 0.01 eV/Å. The bulk rutile with tetragonal symmetry of TiO_2 was cleaved along the (001), (101), (110), and (010) surfaces to form stoichiometric and symmetric slabs. A $2 \times 2 \times 1$ supercell was used for calculations. The slabs thickness were set to four Ti layers, and the vacuum length was 15 Å. The bottom Ti layer was fixed while the other three Ti layers were allowed to relax. The optimized lattice parameters are a = 18.41 Å, b = 9.20 Å, c = 20.16 Å and $\alpha = \beta = 90.00°$, $\gamma = 90.32°$ for (001), a = 21.85 Å, b = 9.18 Å, c = 23.97 Å, and $\alpha = \beta = \gamma = 90.00°$ for (101), a = 11.80 Å, b = 12.99 Å, c = 24.45 Å, and $\alpha = \beta = \gamma = 90.00°$ for (110), and a = 11.76Å, b = 9.51 Å, c = 31.12 Å and $\alpha = \beta = \gamma = 90.00°$ for (010). After complete optimization of slabs, we chose the Ti metal atom as an active site on the surface and the OER intermediates (OH*, $O^{(d)}$, $O^{(p)}$, and OOH*) were adsorbed at a Ti-O bond length of 2.00 Å and again allowed to relax. For sampling the Brillouin zone, a Γ-centered $3 \times 2 \times 1$ k-point mesh was used based on the Monkhorst-Pack scheme.[86] All reported energetics and electronic density of states were calculated using HSE06.[87] Photoexcitation is accounted for as an initial potential provided by the photoexcited electron in the first reaction step as explained in the scheme for free energy profile calculations for OER given in the SI.

3. Results and Discussion

The rutile polymorph of titania is composed of TiO_6 octahedra, which are arranged to form edge-sharing chains along the [001] direction and are corner-sharing in the (001) plane. The surface orientations determine how these octahedra are cut at each of the four low-index Miller surfaces (110), (101), (010), and (001) (Figure 1) resulting in a variation of local geometry and coordination number for the stoichiometric surface atoms. On the lowest energy rutile surface, (110) (Figure 1), half of the Ti atoms are five-coordinated ($^{[5]}$Ti, where $^{[n]}$A is a n-coordinated atom of A) and the other half are $^{[6]}$Ti along the [001] surface rows, these $^{[6]}$Ti have additional bridging surface oxygen atoms ($^{[2]}$O) joining them, completing their octahedral coordination. In contrast, the rutile (010) surface has only $^{[5]}$Ti atoms, with surface
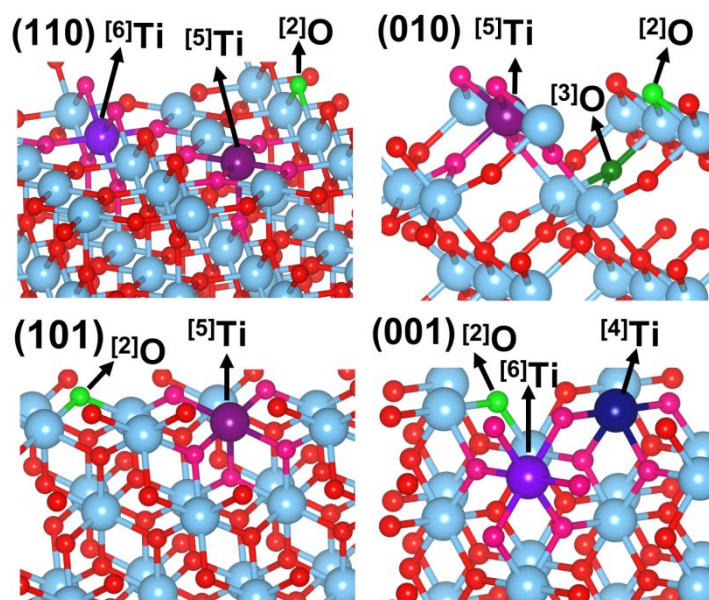
Figure 1. Rutile (110), (010), (101), and (001) surfaces and surface atom coordination (dark blue [4]Ti, dark purple [5]Ti, light purple [6]Ti, and bright green [2]O, dark green [3]O) on each. Red atoms are O and light blue are Ti.

[2]O atoms bridging them (Figure 1). On the (110) surface the bridging Ti–O bonds are perpendicular to the surface plane while on the (010) surface the bridging oxygens are inclined at an angle to the surface (61° in the relaxed stoichiometric structure). The (101) surface also has only [5]Ti with bridging [2]O. However, while on both the (010) and (101) surfaces the [5]Ti lie at the center of the base TiO_5 square pyramids that are slanted from the surface normal. On the (101) surface the (–O–Ti–O–Ti–) chains are zigzagged along the $[10\bar{1}]$ direction, giving the TiO_5 square pyramids alternating tilts (Figure 1). When truncated to the (101) surface, the bulk TiO_6 octahedra form rows where long and short Ti–O bonds have been removed, forming chains of alternating enantiomeric Ti surface sites. The (001) surface exhibits alternating O and Ti rows in the [110] direction, with alternating [6]Ti and [4]Ti (Figure 1). The [6]Ti surface metal sites occupy the center of TiO_6 octahedra, whereas the elimination of two oxygen atoms leads to the relaxation of the octahedron to a distorted tetrahedral [4]Ti. Each (001) surface O atom is bonded to one [4]Ti and one [6]Ti. The diverse coordination of Ti and O is known to result in a range of surface energies; (110) < (010) < (101) < (001),[17,38] matching well with the formation energies per atom of each unit cell (Table S8). The density of states (DoS, Figure S6) of each surface show that their valence bands are all composed of O (2p) orbitals and their conduction bands are mostly comprised of Ti (3d) orbitals. In addition, all of the plots showed a shift in the Fermi energy (E_f) toward the valence band edge with a typical rutile band gap of ~ 3 eV.

Here we directly measure the effect of surface chemistry on water-splitting catalytic properties. The multistep proton-coupled electron transfer (PCET) processes for one-, two-,

and four-electron transfer reactions (eqns. 1-3) are considered for each surface. The (110) surface has been well explored[19,21,23–31] and is included here for direct comparison, but all the results are consistent with previous DFT studies on the bare surface. The detailed PCET mechanism is shown in Section 1 of the SI. For both the peroxo and dangling oxygen mechanisms the free energies of OH* and O* were calculated (Table 1). It is striking that the lowest possible energy mechanism on all the facets goes through the surface-bound peroxo O* (Table 1), denoted as O$^{(p)}$. This is important as this mechanism is often overlooked in favor
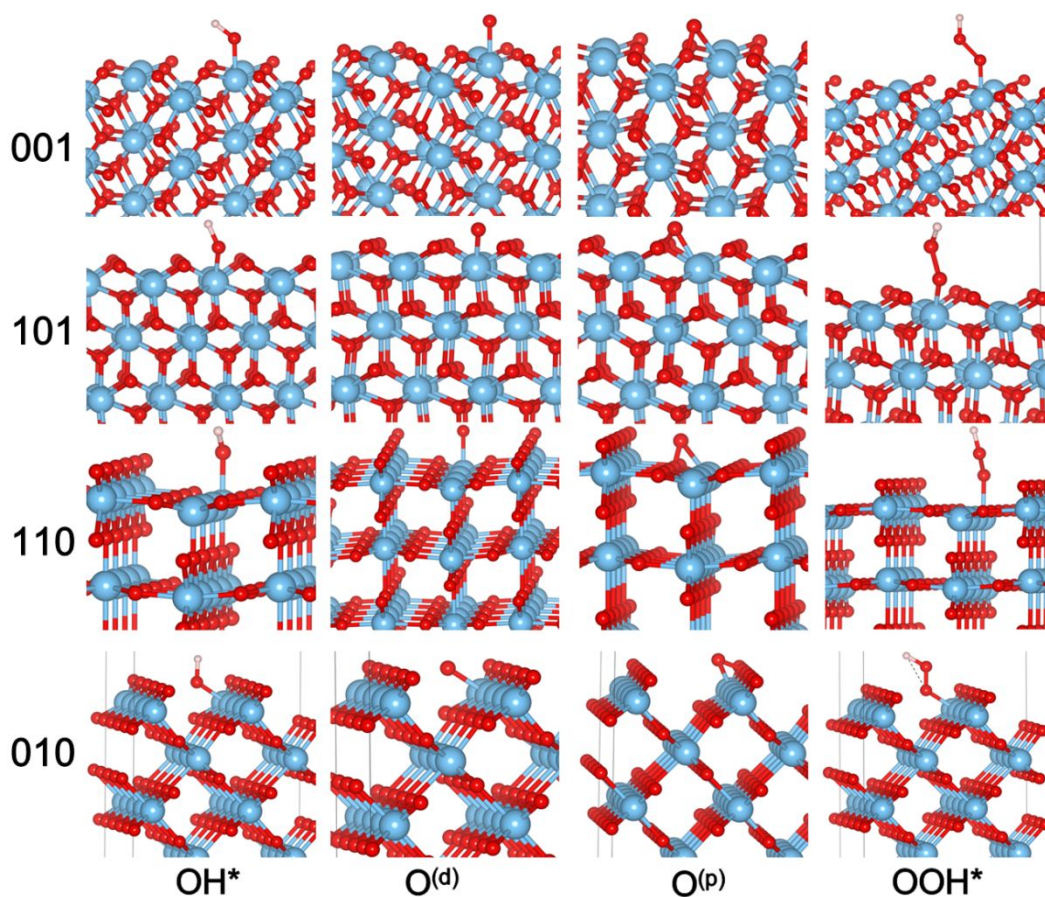

Figure 2. Optimized structures of Rutile (110), (010), (101), and (001) their four possible OER intermediates.

of the similar but less plausible dangling O* intermediate, signified as O$^{(d)}$ (Figure 2). The formation energy of each intermediate adsorbed on the surfaces is within DFT error of the surface formation energy and about 2xs (~ − 4.5 eV) more favorable than the dissociation energy of water (5.15 eV).

For O$_2$ evolution, the rate-determining step is *OH for the (001), (101), and (110) surfaces, whereas, the rate on (010) is determined through the last O$_2$ evolution. The surface adsorption

of OH* is the first step in OER, and its energy and charge transfer (as determined by a ~ 0.41 to 0.48 e$^-$ Bader charge, Table S6) remains the same for all mechanisms. This step is lowest in energy on the (010) surface at 1.04 eV. Loss of the proton to generate O* is the branching point for the O$^{(d)}$ vs. O$^{(p)}$ mechanisms (each mechanism is labeled as surface$^{(intermediate)}$). Each mechanism only has one newly adsorbed surface oxygen, however in the peroxo mechanism the O* forms a bond with an existing surface oxygen. O$^{(p)}$ formation is more favorable for all facets and is significantly lower in energy on (010) (~ 1 eV) than all the other surfaces. This is probably due to the charge transfer to the dangling O$^{(d)}$ intermediates as compared to the newly adsorbed oxygen in the peroxo O$^{(p)}$ intermediates, thus lowering the binding energies of the peroxo mechanism. Interestingly, some of the peroxo O* charge seems to be shared with its bonded surface oxygen (Table S6) proving that peroxo specie is preferable on defect-free TiO$_2$ surface which is in good agreement with previous studies [23,24].

Adsorption of a second OH leading to an OOH* depends on the energy and mechanism of the O* step. The observed charge transfer is ~ 0.94 to 1.49 to the OOH* on all surfaces. Interestingly, the dangling mechanism on the (010) and (110) surfaces has a downhill OOH* step. This however isn't enough to make the dangling mechanism more favorable overall. While the step energies for the two mechanisms are very different (Table S3), according to Sabatier's principle[88] of reactivity, catalytic activity is actually a balance between strong and weak interactions between the substrate and the catalyst.

Table 1. Free energies relative to the resting state '* + 2H$_2$O' for (ΔG$_*$), 'OH*' (ΔG$_{OH*}$), O$^{(d)}$ (ΔG$_O{}^{(d)}$), O$^{(p)}$ (ΔG$_O{}^{(p)}$), OOH* (ΔG$_{OOH*}$), and O$_2$ (ΔG$_{O2}$) and overpotentials 'η' through four-, two- and one-electron (O$_2$/ H$_2$O$_2$ /•OH evolution) processes for all surfaces and mechanisms, labeled surface$^{(intermediate)}$. The rate-limiting step for each mechanism is bolded.

Mechanism	ΔG$_{OH*}$	ΔG$_O{}^{(d)}$	ΔG$_O{}^{(p)}$	ΔG$_{OOH*}$	ΔG$_{O2}$	Product	R.D.S	η (V) 1e$^-$	η (V) 2e$^-$	η (V) 4e$^-$
001$^{(d)}$	**2.99**	5.19	–	6.02	4.92	•OH	OH*	1.76	–	–
001$^{(p)}$	**2.99**	–	4.72	6.02	4.92	•OH	OH*	1.76	–	–
101$^{(d)}$	2.13	**4.66**	–	5.47	4.92	H$_2$O$_2$	O*	–	0.77	1.30
101$^{(p)}$	**2.13**	–	4.01	5.47	4.92	H$_2$O$_2$	OH*	–	0.37	0.90
110$^{(d)}$	1.99	**4.55**	–	4.48	4.92	H$_2$O$_2$	O*	–	0.80	1.33
110$^{(p)}$	**1.99**	–	3.64	4.48	4.92	H$_2$O$_2$	OH*	–	0.23	0.76
010$^{(d)}$	1.04	**3.40**	–	3.16	4.92	O$_2$	O*	–	–	1.13
010$^{(p)}$	1.04	–	1.76	3.16	**4.92**	O$_2$	O$_2$	–	–	0.53

For the •OH formation 1-electron process, all of the surfaces have the same overpotential. For the H$_2$O$_2$ formation 2-electron process, 110$^{(p)}$ has the lowest overpotential of 0.23 V,

followed by $101^{(p)}$ at 0.37 V with OH* as the rate-limiting step, for both. Four-electron O_2 evolution through the $010^{(p)}$ has the least overpotential of 0.53 V. Interestingly, among all surfaces (010) showed highest charge transfer from surface to intermediates supporting high photocatalytic activity of this surface.

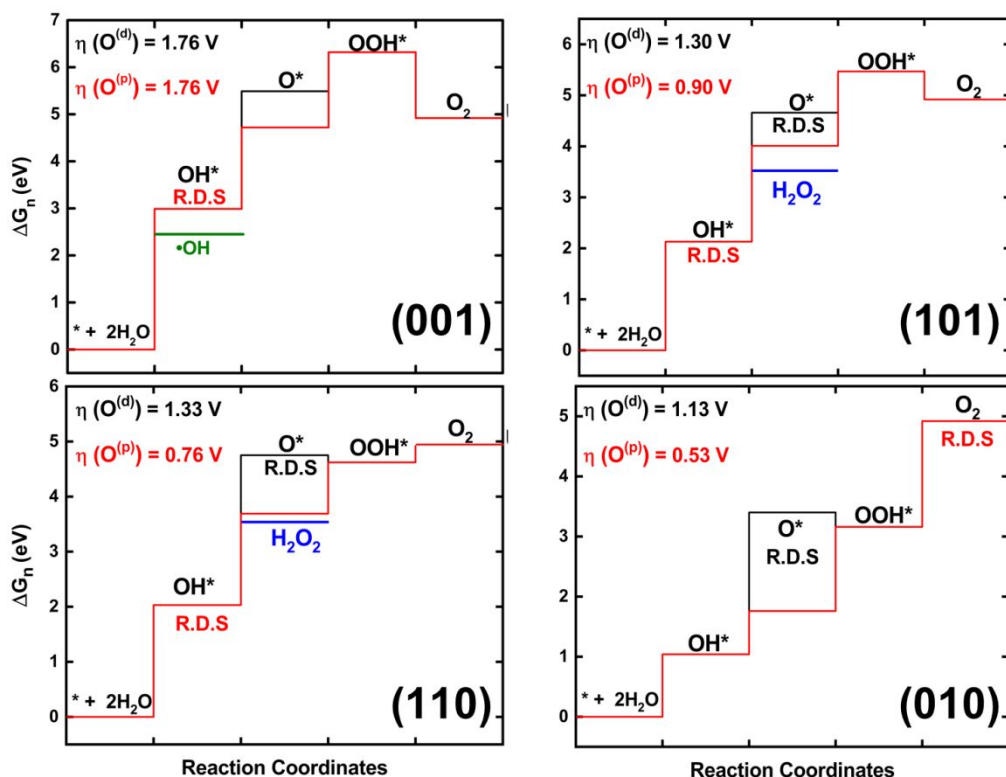The product selectivity map[20,21] (Figure 4) compares the relative free energies of OH* and

Figure 3. Free energy profiles and overpotential of OER on stoichiometric (001), (101), (110), and (010) rutile through dangling $O^{(d)}$ (black) and peroxo $O^{(p)}$ (red) intermediates under no external potential. The rate-determining step (R.D.S.) is marked and H_2O_2 formation (blue) and •OH formation (green) are shown for relevant surfaces.
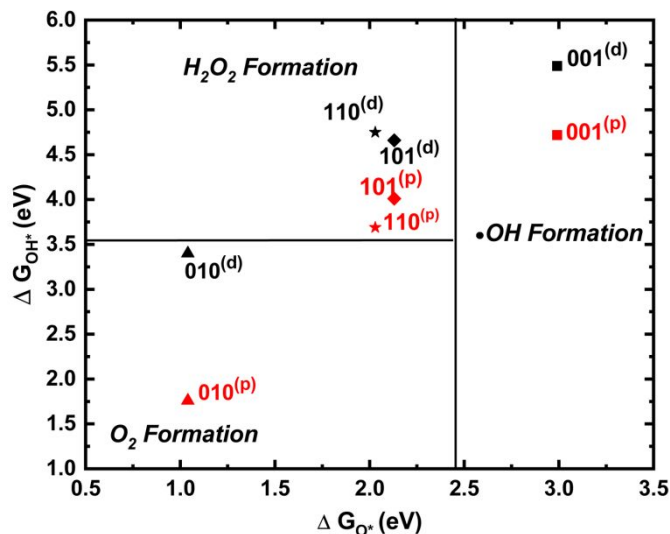
Figure 4. Phase diagram for product selectivity for rutile (001), (101), (110), and (010) surfaces. Black and red show dangling and peroxo mechanisms, respectively.

O* to the reaction equilibrium potentials for H_2O_2, O_2, and $\cdot OH$ formation. None of the surfaces predict a different product for the two mechanisms. Instead, $\cdot OH$ formation is favored on (001), H_2O_2 formation for (110) and (101), while only O_2 evolution is preferred for (001). Interestingly, rutile 110$^{(p)}$ is adjoining the O_2 evolution boundary, indicating that with very little added energy (110) could evolve O_2. Importantly, under irradiation, the redox potential of photogenerated holes in the valence band is almost equal to the band gap (over ~3 eV) making all three mechanisms (1e$^-$, 2e$^-$, and 4e$^-$) realistic on all these surfaces. Water oxidation gates most easily on (110) and (101) through the formation of H_2O_2. On the (001) surface however $\cdot OH$ formation likely makes the surface unproductive for O_2 evolution.

Because these reactions occur in the presence of water and involve protons moving at many steps, pH plays a role in the reactivity. In particular, the energy of every step is modulated by pH. By using a pH-dependent reference electrode, the calculated overpotential can directly account for the effect of pH on surface reactivity.[17,21,89–91] While a pH of 14 (pH = 0 in Table 1) alters the binding energies of the reaction intermediates (Table S3) and affects the threshold values for the 1e$^-$, 2e$^-$, and 4e$^-$ processes, it does not affect the selectivity and overpotential of OER on each surface.

Volcano plots have been extensively used for the analysis of OER activity of different oxide systems.[92–94] $\Delta G_{O*} - \Delta G_{OH*}$ provides a computational metric of OER
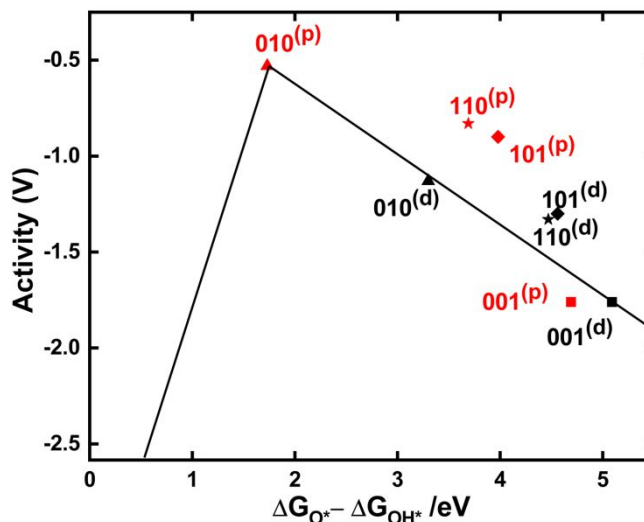

Figure 5. Volcano plot (-η vs. $\Delta G_{O*} - \Delta G_{OH*}$) for the oxygen evolution reaction on low-indexed TiO_2 surfaces explored in this study. The data points are grouped with black color for dangling O$^{(d)}$ and red color for peroxo O$^{(p)}$.

activity[95] that can predict the activity of various catalysts. Plotting the negative value of calculated overpotential (–η, activity) as a function of this metric for each of the facets considered here leads to a volcanic relationship (Figure 5). The top of the volcano shows the best OER activity with the lowest overpotential for 010$^{(p)}$. It is clear in the volcano plot that the overpotential depends strongly on the mechanism for each surface, *i.e.* O$^{(d)}$ or O$^{(p)}$. Among all the facets (001) results in the highest overpotential indicating that this facet is least active for water oxidation. This is in good agreement with previous studies that show (001) is unstable, with high surface energy and experimental reconstruction.[96–98] However, these results show clearly that other low-indexed facets, beyond the well-studied (110), should be considered for water oxidation. In particular, 010$^{(p)}$ is more reactive and 101$^{(p)}$ is almost as reactive as than 110$^{(p)}$.

4. Conclusions:

This work provides the first direct calculations of water oxidation on low-index rutile TiO$_2$ facets, (001), (101), and (101), using DFT. This work provides new insights into water oxidation mechanisms and reactivity of various low-index Miller facets of rutile TiO$_2$. In particular, water oxidation proceeds through the peroxo intermediate on all of these stoichiometric facets. The (001) facet resulted in high overpotential for OER leading to •OH radical formation. A two-electron process to produce H$_2$O$_2$ is favored on the (101) and (110) facets with fairly low overpotentials, ~ 0.3 V, for OER. The only facet that prefers direct OER is (010), with an overpotential of 0.53 V. These results are supported via a volcano plot which predicts the high activity of a peroxo mechanism of OER on the (010) facet. Critically, these results show that facets beyond the well-studied (110) may play a role in measured reactivity and should be explored further to better understand the effect of surface coverage and oxygen vacancies.

References:

1   K. Maeda and K. Domen, New non-oxide photocatalysts designed for overall water splitting under visible light, *The journal of physical chemistry C*, 2007, **111**, 7851–7861.

2   A. Kudo and Y. Miseki, Heterogeneous photocatalyst materials for water splitting, *Chem Soc Rev*, 2009, **38**, 253–278.

3   K. Maeda and K. Domen, Photocatalytic water splitting: recent progress and future challenges, *J Phys Chem Lett*, 2010, **1**, 2655–2661.

4   J. Schneider and D. W. Bahnemann, Undesired Role of Sacrificial Reagents in Photocatalysis, *J Phys Chem Lett*, 2013, **4**, 3479–3483.

5   S. Wang, G. Liu and L. Wang, Crystal facet engineering of photoelectrodes for photoelectrochemical water splitting, *Chem Rev*, 2019, **119**, 5192–5247.

6   W. Li, K. R. Yang, X. Yao, Y. He, Q. Dong, G. W. Brudvig, V. S. Batista and D. Wang, Facet-dependent kinetics and energetics of hematite for solar water oxidation reactions, *ACS Appl Mater Interfaces*, 2018, **11**, 5616–5622.

7   R. Li, F. Zhang, D. Wang, J. Yang, M. Li, J. Zhu, X. Zhou, H. Han and C. Li, Spatial separation of photogenerated electrons and holes among {010} and {110} crystal facets of BiVO$_4$, *Nat Commun*, 2013, **4**, 1–7.

8   C. Li, C. Koenigsmann, W. Ding, B. Rudshteyn, K. R. Yang, K. P. Regan, S. J. Konezny, V. S. Batista, G. W. Brudvig and C. A. Schmuttenmaer, Facet-dependent photoelectrochemical performance of TiO$_2$ nanostructures: an experimental and computational study, *J Am Chem Soc*, 2015, **137**, 1520–1529.

9   V. I. M. J. R. Ram-Mohan, LR 2001 Band parameters for III-V compound semiconductors and their alloys, *J. Appl. Phys*, **89**, 5815.

10   O. Madelung, *Semiconductors: data handbook*, Springer Science & Business Media, 2004.

11   A. L. Linsebigler, G. Lu and J. T. Yates Jr, Photocatalysis on TiO$_2$ surfaces: principles, mechanisms, and selected results, *Chem Rev*, 1995, **95**, 735–758.

12   M. A. Henderson and I. Lyubinetsky, Molecular-level insights into photocatalysis from scanning probe microscopy studies on TiO$_2$ (110), *Chem Rev*, 2013, **113**, 4428–4455.

13   T. L. Thompson and J. T. Yates, Surface science studies of the photoactivation of TiO$_2$ new photochemical processes, *Chem Rev*, 2006, **106**, 4428–4453.

14   D. C. Cronemeyer, Infrared Absorption of Reduced Rutile TiO$_2$ Single Crystals, *Physical Review*, 1959, **113**, 1222–1226.

15   N. Tian, Z.-Y. Zhou, S.-G. Sun, Y. Ding and Z. L. Wang, Synthesis of tetrahexahedral platinum nanocrystals with high-index facets and high electro-oxidation activity, *Science*, 2007, **316**, 732–735.

16   C. Xu, F. Xu, X. Chen, Z. Li, Z. Luan, X. Wang, Q. Guo and X. Yang, Wavelength-Dependent Water Oxidation on Rutile TiO$_2$ (110), *J Phys Chem Lett*, 2021, **12**, 1066–1072.

17   A. Imanishi, T. Okamura, N. Ohashi, R. Nakamura and Y. Nakato, Mechanism of Water Photooxidation Reaction at Atomically Flat TiO_2 (Rutile) (110) and (100) Surfaces: Dependence on Solution pH, *J Am Chem Soc*, 2007, **129**, 11569–11578.

18   H. Perron, C. Domain, J. Roques, R. Drot, E. Simoni and H. Catalette, Optimisation of accurate rutile TiO_2 (110),(100),(101) and (001) surface models from periodic DFT calculations, *Theor Chem Acc*, 2007, **117**, 565–574.

19   Á. Valdés, Z.-W. Qu, G.-J. Kroes, J. Rossmeisl and J. K. Nørskov, Oxidation and Photo-Oxidation of Water on TiO_2 Surface, *The Journal of Physical Chemistry C*, 2008, **112**, 9872–9879.

20   S. Siahrostami, G.-L. Li, V. Viswanathan and J. K. Nørskov, One- or Two-Electron Water Oxidation, Hydroxyl Radical, or H_2O_2 Evolution, *J Phys Chem Lett*, 2017, **8**, 1157–1160.

21   A. S. Malik, T. Liu, M. Dupuis, R. Li and C. Li, Water Oxidation on TiO_2: A Comparative DFT Study of $1e^-$, $2e^-$, and $4e^-$ Processes on Rutile, Anatase, and Brookite, *The Journal of Physical Chemistry C*, 2020, **124**, 8094–8100.

22   J. Rossmeisl, Z.-W. Qu, H. Zhu, G.-J. Kroes and J. K. Nørskov, Electrolysis of water on oxide surfaces, *Journal of Electroanalytical Chemistry*, 2007, **607**, 83–89.

23   U. Diebold, The surface science of titanium dioxide, *Surf Sci Rep*, 2003, **48**, 53–229.

24   C. L. Pang, R. Lindsay and G. Thornton, Chemical reactions on rutile TiO_2 (110), *Chem Soc Rev*, 2008, **37**, 2328–2353.

25   X. Yin, M. Calatayud, H. Qiu, Y. Wang, A. Birkner, C. Minot and C. Wöll, Diffusion versus desorption: complex behavior of H Atoms on an oxide surface, *ChemPhysChem*, 2008, **9**, 253–256.

26   P. M. Kowalski, B. Meyer and D. Marx, Composition, structure, and stability of the rutile TiO_2 (110) surface: Oxygen depletion, hydroxylation, hydrogen migration, and water adsorption, *Phys Rev B*, 2009, **79**, 115410.

27   A. Sasahara, T. Murakami and M. Tomitori, XPS and STM study of TiO_2 (110)-(1× 1) surfaces immersed in simulated body fluid, *Surf Sci*, 2018, **668**, 61–67.

28   X. Yu, Z. Zhang, C. Yang, F. Bebensee, S. Heissler, A. Nefedov, M. Tang, Q. Ge, L. Chen and B. D. Kay, Interaction of formaldehyde with the Rutile TiO_2 (110) Surface: A combined experimental and theoretical study, *The Journal of Physical Chemistry C*, 2016, **120**, 12626–12636.

29   D. Zhang, M. Yang and S. Dong, Hydroxylation of the rutile TiO_2 (110) surface enhancing its reducing power for photocatalysis, *The Journal of Physical Chemistry C*, 2015, **119**, 1451–1456.

30   A. Imanishi, E. Tsuji and Y. Nakato, Dependence of the work function of TiO_2 (Rutile) on crystal faces, studied by a scanning auger microprobe, *The Journal of Physical Chemistry C*, 2007, **111**, 2128–2132.

31   D. Wang, T. Sheng, J. Chen, H.-F. Wang and P. Hu, Identifying the key obstacle in photocatalytic oxygen evolution on rutile TiO_2, *Nat Catal*, 2018, **1**, 291–299.

32   T. v Perevalov and V. A. Gritsenko, Electronic structure of TiO_2 rutile with oxygen vacancies: Ab initio simulations and comparison with the experiment, *Journal of Experimental and Theoretical Physics*, 2011, **112**, 310–316.

33   B. J. Morgan and G. W. Watson, A DFT+ U description of oxygen vacancies at the TiO_2 rutile (1 1 0) surface, *Surf Sci*, 2007, **601**, 5034–5041.

34   S. Wendt, R. Schaub, J. Matthiesen, E. K. Vestergaard, E. Wahlström, M. D. Rasmussen, P. Thostrup, L. M. Molina, E. Lægsgaard and I. Stensgaard, Oxygen vacancies on TiO_2 (1 1 0) and their interaction with H_2O and O_2: A combined high-resolution STM and DFT study, *Surf Sci*, 2005, **598**, 226–245.

35   G. Mattioli, F. Filippone, P. Alippi and A. A. Bonapasta, Ab initio study of the electronic states induced by oxygen vacancies in rutile and anatase TiO_2, *Phys Rev B*, 2008, **78**, 241201.

36   M. Elahifard, M. R. Sadrian, A. Mirzanejad, R. Behjatmanesh-Ardakani and S. Ahmadvand, Dispersion of defects in TiO_2 semiconductor: Oxygen vacancies in the bulk and surface of rutile and anatase, *Catalysts*, 2020, **10**, 397.

37   N. G. Petrik and G. A. Kimmel, Reaction kinetics of water molecules with oxygen vacancies on rutile TiO_2 (110), *The Journal of Physical Chemistry C*, 2015, **119**, 23059–23067.

38   B. J. Morgan and G. W. Watson, A density functional theory+ U study of oxygen vacancy formation at the (110),(100),(101), and (001) surfaces of rutile TiO_2, *The Journal of Physical Chemistry C*, 2009, **113**, 7322–7328.

39   A. Tilocca and A. Selloni, O_2 and vacancy diffusion on rutile (110): pathways and electronic properties, *ChemPhysChem*, 2005, **6**, 1911–1916.

40   R. Schaub, P. Thostrup, N. Lopez, E. Lægsgaard, I. Stensgaard, J. K. Nørskov and F. Besenbacher, Oxygen vacancies as active sites for water dissociation on rutile TiO_2 (110), *Phys Rev Lett*, 2001, **87**, 266104.

41   Y. Yamamoto, S. Kasamatsu and O. Sugino, Scaling relation of oxygen reduction reaction intermediates at defective TiO_2 surfaces, *The Journal of Physical Chemistry C*, 2019, **123**, 19486–19492.

42   M.-C. Tsai, T.-T. Nguyen, N. G. Akalework, C.-J. Pan, J. Rick, Y.-F. Liao, W.-N. Su and B.-J. Hwang, Interplay between molybdenum dopant and oxygen vacancies in a TiO_2 support enhances the oxygen reduction reaction, *ACS Catal*, 2016, **6**, 6551–6559.

43   L. Mino, C. Negri, R. Santalucia, G. Cerrato, G. Spoto and G. Martra, Morphology, Surface Structure and Water Adsorption Properties of TiO_2 Nanoparticles: A Comparison of Different Commercial Samples., *Molecules*, , DOI:10.3390/molecules25204605.

44   S. Siahrostami and A. Vojvodic, Influence of Adsorbed Water on the Oxygen Evolution Reaction on Oxides, *The Journal of Physical Chemistry C*, 2015, **119**, 1032–1037.

45   Y. Adachi, Y. Sugawara and Y. J. Li, Atomic Scale Three-Dimensional Au Nanocluster on a Rutile TiO_2 (110) Surface Resolved by Atomic Force Microscopy, *J Phys Chem Lett*, 2020, **11**, 7153–7158.

46   R. S. Haider, S. Wang, Y. Gao, A. S. Malik, N. Ta, H. Li, B. Zeng, M. Dupuis, F. Fan and C. Li, Boosting photocatalytic water oxidation by surface plasmon resonance of Ag_xAu_{1-x} alloy nanoparticles, *Nano Energy*, 2021, **87**, 106189.

47   A. S. Malik, T. Liu, M. Rittiruam, T. Saelee, J. L. F. da Silva, S. Praserthdam and P. Praserthdam, On a high photocatalytic activity of high-noble alloys Au–Ag/TiO_2 catalysts during oxygen evolution reaction of water oxidation, *Sci Rep*, 2022, **12**, 2604.

48   M. Nolan, Alkaline earth metal oxide nanocluster modification of rutile TiO_2 (110) promotes water activation and CO_2 chemisorption, *J Mater Chem A Mater*, 2018, **6**, 9451–9466.

49   B. J. Hwang, W.-N. Su, B.-J. Shieh and M.-C. Tsai, in *ECS Meeting Abstracts*, IOP Publishing, 2017, p. 1585.

50   M. García-Mota, A. Vojvodic, H. Metiu, I. C. Man, H. Su, J. Rossmeisl and J. K. Nørskov, Tailoring the Activity for Oxygen Evolution Electrocatalysis on Rutile TiO_2 (110) by Transition-Metal Substitution, *ChemCatChem*, 2011, **3**, 1607–1611.

51   T. Ohno, K. Sarukawa and M. Matsumura, Crystal faces of rutile and anatase TiO_2 particles and their roles in photocatalytic reactions, *New Journal of Chemistry*, 2002, **26**, 1167–1170.

52   F. Lindberg, J. Heinrichs, F. Ericson, P. Thomsen and H. Engqvist, Hydroxylapatite growth on single-crystal rutile substrates, *Biomaterials*, 2008, **29**, 3317–3323.

53   O. Warschkow, Y. Wang, A. Subramanian, M. Asta and L. D. Marks, Structure and local-equilibrium thermodynamics of the c (2×2) reconstruction of rutile TiO_2 (100), *Phys Rev Lett*, 2008, **100**, 086102.

54   Y. Lu, B. Jaeckel and B. A. Parkinson, Preparation and characterization of terraced surfaces of low-index faces of anatase, rutile, and brookite, *Langmuir*, 2006, **22**, 4472–4475.

55   X. Zhou, Z. Wang, X. Xia, G. Shao, K. Homewood and Y. Gao, Synergistic cooperation of rutile TiO_2 {002},{101}, and {110} facets for hydrogen sensing, *ACS Appl Mater Interfaces*, 2018, **10**, 28199–28209.

56   X. Yang, C. Jin, C. Liang, D. Chen, M. Wu and C. Y. Jimmy, Nanoflower arrays of rutile TiO_2, *Chemical Communications*, 2011, **47**, 1184–1186.

57   Y. Yamamoto, Y. Matsumoto and H. Koinuma, Homo-epitaxial growth of rutile TiO_2 film on step and terrace structured substrate, *Appl Surf Sci*, 2004, **238**, 189–192.

58   B. D. Sosnowchik, H. C. Chiamori, Y. Ding, J.-Y. Ha, Z. L. Wang and L. Lin, Titanium dioxide nanoswords with highly reactive, photocatalytic facets, *Nanotechnology*, 2010, **21**, 485601.

59   G. E. Poirier, B. K. Hance and J. M. White, Identification of the facet planes of phase I TiO_2 (001) rutile by scanning tunneling microscopy and low energy electron diffraction, *Journal of Vacuum Science & Technology B: Microelectronics and Nanometer Structures Processing, Measurement, and Phenomena*, 1992, **10**, 6–15.

60   H. Nörenberg, F. Dinelli and G. A. D. Briggs, Network-like (72× 2) R45° surface reconstruction on rutile TiO_2 (001) by non-equilibrium self-organization, *Surf Sci*, 1999, **436**, L635–L640.

61   J. Muscat and N. M. Harrison, The physical and electronic structure of the rutile (001) surface, *Surf Sci*, 2000, **446**, 119–127.

62   L. Wu, J. Lin, L. Ren, Q. Li, X. Chi, L. Luo, Y. Zhang and M.-H. Zeng, Electronic structures of hydroxylated low index surfaces of rutile and anatase-type titanium dioxide, *Physical Chemistry Chemical Physics*, 2022, **24**, 15091–15102.

63   U. Terranova and D. R. Bowler, Adsorption of Catechol on TiO_2 Rutile (100): A Density Functional Theory Investigation, *The Journal of Physical Chemistry C*, 2010, **114**, 6491–6495.

64   E. German, R. Faccio and Á. W. Mombrú, Theoretical study of new potential semiconductor surfaces performance for dye sensitized solar cell usage: TiO_2-B (001), (100) and H2Ti3O7 (100), *Appl Surf Sci*, 2017, **426**, 1182–1189.

65   P. Jones and J. A. Hockey, Infra-red studies of rutile surfaces. Part 2.—hydroxylation, hydration and structure of rutile surfaces, *Transactions of the Faraday Society*, 1971, **67**, 2679–2685.

66   M. Xu, S. Shao, B. Gao, J. Lv, Q. Li, Y. Wang, H. Wang, L. Zhang and Y. Ma, Anatase (101)-like structural model revealed for metastable rutile TiO_2 (011) surface, *ACS Appl Mater Interfaces*, 2017, **9**, 7891–7896.

67   Y. Wang, S. Lee, P. Vilmercati, H. N. Lee, H. H. Weitering and P. C. Snijders, Atomically flat reconstructed rutile TiO_2 (001) surfaces for oxide film growth, *Appl Phys Lett*, 2016, **108**, 091604.

68   U. Diebold, J. Lehman, T. Mahmoud, M. Kuhn, G. Leonardelli, W. Hebenstreit, M. Schmid and P. Varga, Intrinsic defects on a TiO_2 (110)(1× 1) surface and their reaction with oxygen: a scanning tunneling microscopy study, *Surf Sci*, 1998, **411**, 137–153.

69   S. Fischer, A. W. Munz, K.-D. Schierbaum and W. Göpel, The geometric structure of intrinsic defects at TiO_2 (110) surfaces: an STM study, *Surf Sci*, 1995, **337**, 17–30.

70   C. Xu, X. Lai, G. W. Zajac and D. W. Goodman, Scanning tunneling microscopy studies of the TiO_2 (110) surface: structure and the nucleation growth of Pd, *Phys Rev B*, 1997, **56**, 13464.

71   K. P. Maenetja and P. E. Ngoepe, Unravelling the Catalytic Activity of MnO_2, TiO_2, and VO_2 (110) Surfaces by Oxygen Coadsorption on Sodium-Adsorbed MO_2 {M= Mn, Ti, V}, *ACS Omega*, 2022, **7**, 25991–25998.

72   Y.-F. Li, U. Aschauer, J. Chen, A. Selloni, J. F. Montoya, D. W. Bahnemann, P. Salvador, J. Peral, M. Setvin, U. Aschauer, J. Hulva, T. Simschitz, B. Daniel, M. Schmid, A. Selloni, U. Diebold, I. Sokolović, M. Reticcioli, M. Čalkovský, M. Wagner, M. Schmid, C. Franchini, U. Diebold and M. Setvín, Catalytic role of bridging oxygens in TiO_2 liquid phase photocatalytic reactions: analysis of H_2O_{16} photooxidation on labeled $Ti_{18}O_2$, *Catal Sci Technol*, 2017, **138**, 9565–9571.

73   L. Hou, M. Zhang, Z. Guan, Q. Li and J. Yang, Effect of annealing ambience on the formation of surface/bulk oxygen vacancies in TiO_2 for photocatalytic hydrogen evolution, *Appl Surf Sci*, 2018, **428**, 640–647.

74   C. Xiao, B.-A. Lu, P. Xue, N. Tian, Z.-Y. Zhou, X. Lin, W.-F. Lin and S.-G. Sun, High-Index-Facet- and High-Surface-Energy Nanocrystals of Metals and Metal Oxides as Highly Efficient Catalysts, *Joule*, 2020, **4**, 2562–2598.

75   A. Valdes and G.-J. Kroes, First principles study of the photo-oxidation of water on tungsten trioxide (WO_3), *J Chem Phys*, 2009, **130**, 114701.

76   R. Kishore, X. Cao, X. Zhang and A. Bieberle-Hütter, Electrochemical water oxidation on WO_3 surfaces: A density functional theory study, *Catal Today*, 2019, **321**, 94–99.

77   C. Shao, A. S. Malik, J. Han, D. Li, M. Dupuis, X. Zong and C. Li, Oxygen vacancy engineering with flame heating approach towards enhanced photoelectrochemical water oxidation on WO_3 photoanode, *Nano Energy*, 2020, **77**, 105190.

78   E. Jossou, L. Malakkal, N. Y. Dzade, A. Claisse, B. Szpunar and J. Szpunar, DFT + U Study of the Adsorption and Dissociation of Water on Clean, Defective, and Oxygen-Covered U_3Si_2{001}, {110}, and {111} Surfaces, *The Journal of Physical Chemistry C*, 2019, **123**, 19453–19467.

79   H. Ouhbi and U. Aschauer, Water oxidation catalysis on reconstructed $NaTaO_3$ (001) surfaces, *J Mater Chem A Mater*, 2019, **7**, 16770–16776.

80   S. Hammes-Schiffer and A. A. Stuchebrukhov, Theory of Coupled Electron and Proton Transfer Reactions, *Chem Rev*, 2010, **110**, 6939–6960.

81   A. Bard, *Standard potentials in aqueous solution*, Routledge, 2017.

82   D. A. Armstrong, R. E. Huie, S. Lymar, W. H. Koppenol, G. Merényi, P. Neta, D. M. Stanbury, S. Steenken and P. Wardman, Standard electrode potentials involving radicals in aqueous solution: inorganic radicals, *Bioinorg React Mech*, 2013, **9**, 59–61.

83   J. P. Perdew, K. Burke and M. Ernzerhof, Generalized gradient approximation made simple, *Phys Rev Lett*, 1996, **77**, 3865.

84   G. Kresse and J. Furthmüller, Efficient iterative schemes for ab initio total-energy calculations using a plane-wave basis set, *Phys Rev B*, 1996, **54**, 11169.

85   G. Kresse and J. Furthmüller, Efficiency of ab-initio total energy calculations for metals and semiconductors using a plane-wave basis set, *Comput Mater Sci*, 1996, **6**, 15–50.

86   J. I. Rodríguez, P. W. Ayers, A. W. Götz and F. de L. Castillo-Alvarado, Virial theorem in the Kohn–Sham density-functional theory formalism: Accurate calculation of the atomic quantum theory of atoms in molecules energies, *J Chem Phys*, 2009, **131**, 021101.

87   J. Heyd, G. E. Scuseria and M. Ernzerhof, Hybrid functionals based on a screened Coulomb potential, *J Chem Phys*, 2003, **118**, 8207–8215.

88   H. Ooka, J. Huang and K. S. Exner, The sabatier principle in electrocatalysis: Basics, limitations, and extensions, *Front Energy Res*, 2021, **9**, 654460.

89   L. Giordano, B. Han, M. Risch, W. T. Hong, R. R. Rao, K. A. Stoerzinger and Y. Shao-Horn, pH dependence of OER activity of oxides: Current and future perspectives, *Catal Today*, 2016, **262**, 2–10.

90   G. He, M. Zhang and G. Pan, Influence of pH on Initial Concentration Effect of Arsenate Adsorption on TiO_2 Surfaces: Thermodynamic, DFT, and EXAFS Interpretations, *The Journal of Physical Chemistry C*, 2009, **113**, 21679–21686.

91   S. Bendjabeur, R. Zouaghi, B. Zouchoune and T. Sehili, DFT and TD-DFT insights, photolysis and photocatalysis investigation of three dyes with similar structure under UV irradiation with and without TiO_2 as a catalyst: Effect of adsorption, pH and light intensity, *Spectrochim Acta A Mol Biomol Spectrosc*, 2018, **190**, 494–505.

92   K. S. Exner, Overpotential-Dependent Volcano Plots to Assess Activity Trends in the Competing Chlorine and Oxygen Evolution Reactions, *ChemElectroChem*, 2020, **7**, 1448–1455.

93   X. Li, S. Duan, E. Sharman, Y. Zhao, L. Yang, Z. Zhuo, P. Cui, J. Jiang and Y. Luo, Exceeding the volcano relationship in oxygen reduction/evolution reactions using

single-atom-based catalysts with dual-active-sites, *J Mater Chem A Mater*, 2020, **8**, 10193–10198.

94   M. Craig, G. Coulter, E. Dolan, J. Soriano-López, E. Mates-Torres, W. Schmitt and M. García Melchor, Universal scaling relations for the rational design of molecular water oxidation catalysts with near-zero overpotential, *Nat Commun*, , DOI:10.1038/s41467-019-12994-w.

95   I. C. Man, H.-Y. Su, F. Calle-Vallejo, H. A. Hansen, J. I. Martínez, N. G. Inoglu, J. Kitchin, T. F. Jaramillo, J. K. Nørskov and J. Rossmeisl, Universality in Oxygen Evolution Electrocatalysis on Oxide Surfaces, *ChemCatChem*, 2011, **3**, 1159–1165.

96   A. Gomer and T. Bredow, Effect of Doping on Rutile TiO_2 Surface Stability and Crystal Shapes, *ChemistryOpen*, 2022, **11**, e202200077.

97   L. Museur, G. D. Tsibidis, A. Manousaki, D. Anglos and A. Kanaev, Surface structuring of rutile TiO_2 (100) and (001) single crystals with femtosecond pulsed laser irradiation, *Journal of the Optical Society of America B*, 2018, **35**, 2600–2607.

98   B. Wei, F. Tielens and M. Calatayud, Understanding the role of rutile TiO_2 surface orientation on molecular hydrogen activation, *Nanomaterials*, 2019, **9**, 1199.